Niobium Nitride Resonators for Cavity Magnonics Devices

Supriya Mandal,[1,*] Lucky N. Kapoor,[1,*] John Jesudasan,[1] Pratap Raychaudhuri,[1] Vibhor Singh,[2,†] and Mandar M. Deshmukh[1,‡]

[1]*Department of Condensed Matter Physics and Materials Science, Tata Institute of Fundamental Research, Homi Bhabha Road, Mumbai 400005, India*

[2]*Department of Physics, Indian Institute of Science, Bangalore 560012, India*

We investigate the performance of niobium nitride superconducting coplanar waveguide resonators towards hybrid quantum devices with magnon-photon coupling. We find internal quality factors ~ 20000 at 20 mK base temperature, in zero magnetic field. We find that by reducing film thickness below 100 nm internal quality factor greater than 1000 can be maintained up to parallel magnetic field of $\sim$1 T and perpendicular magnetic field of $\sim$100 mT. We demonstrate strong coupling of these resonators with an yttrium iron garnet sphere which suggests that these cavities will serve as a good platform for studying magnon-photon coupling in 2D ferromagnet based hybrid quantum systems.

I. INTRODUCTION

Superconducting coplanar waveguide (SCPW) resonators are of interest as elements of architecture for hybrid quantum systems and quantum computation related studies. The two dimensional (2D) structure, scalability and control over impedance across varying length scales for SCPW provide a natural way to couple them with various mesoscopic systems. They have been used for making kinetic inductance detectors [1], parametric amplifiers [2, 3] and have been coupled to superconducting qubits [4], nano-mechanical resonators [5, 6], spin ensembles [7–9] and quantum dots [10, 11]. They have become an important component for realizing hybrid quantum devices.

For application of SCPW resonators in hybrid quantum devices involving novel systems such as ESR systems [9, 12–14], NV centers [7, 8] and different topological systems [15–17], performance under magnetic field is additionally required. Furthermore, with the advent of 2D magnetic materials [18] and possibility to utilize their unique properties in hybrid quantum designing schemes $\sim$100 mT magnetic fields in arbitrary directions is required. This additional requirement for the SCPW resonators necessitates use of type-II superconductors having high upper critical magnetic field (H_{C_2}) like Mo-Re, TiN, Nb-Ti-N and NbN [19–23]. In the presence of magnetic field, flux vortices are generated in these materials which causes dissipative vortex motion in presence of high frequency oscillatory currents. Moreover, reduction in Cooper pairs due to formation of normal cores of the vortices causes increase in kinetic inductance which effects in decrease in resonance frequency [24]. Control over this kind of vortex induced dissipation can be achieved through introduction of pinning sites to trap the vortices which can either be done by utilizing intrinsic disorder [25] or by fabricating artificial pinning sites [26–28].

Niobium nitride (NbN) is a disordered type-II superconductor with a high transition temperature ($T_C \approx 16.8$ K), high upper critical magnetic field ($H_{C_2} \approx 15$ T), small coherence length (≈ 5 nm) and large penetration depth (≈ 250 nm) [29–31]. NbN thin films of varying thicknesses with moderately high T_C can be realized, which are also stable in ambient condition and robust with respect to thermal cycling from room temperature to cryogenic temperatures. Another interesting property of NbN is that its T_C depends mainly on the carrier density (and not disorder) for samples with $T_C > 10$ K [29]. This makes NbN a potential candidate for reducing dissipation due to vortices by utilizing inherent disorder.

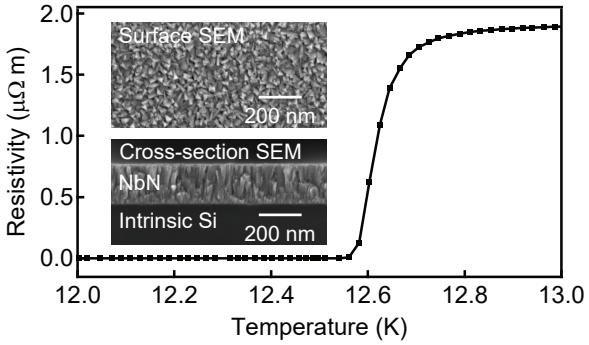

FIG. 1. Variation of resistivity of a 80 nm thick NbN film deposited by sputtering on intrinsic silicon with temperature [Inset: SEM images of top and cross sectional views of an NbN film].

In this work we fabricate and probe the properties of NbN SCPW resonators. Traditionally, SCPW resonators are fabricated by careful substrate surface preparation followed by the deposition of superconducting film. Subsequently, etching processes are used to pattern the resonator. Here we intentionally use a simple lift-off based fabrication process. The motivation behind this approach is two-fold: (a) it helps to establish baseline properties and (b) it opens up the possibility to integrate novel exfoliable materials into microwave circuitry. The NbN SCPW resonators are characterized by investigating the internal quality factor (Q_i) for different drive powers (P_{RF}), temperature (T), and two configurations of the magnetic field (B) primarily for two different thicknesses (t) of the NbN thin film. We find Q_i of $\sim 2 \times 10^4$ at 20 mK and zero magnetic field. We also find that Q_i is higher than 1000 for in-plane

* these authors contributed equally
† Corresponding author; v.singh@iisc.ac.in
‡ Corresponding author; deshmukh@tifr.res.in

fields of $\sim$ 1 T and perpendicular fields of $\sim$ 100 mT. Few 100 mT is often the magnetic field range around which many materials show ferromagnetic, antiferromagnetic and electron spin resonances [32, 33]. For example, using average g-factor of 2.2 for chromium trihalides [34] we find that approximately 160 mT magnetic field is required for resonant coupling of the magnons in these materials with microwave photons in a resonator with resonance frequency around 5 GHz. This makes NbN SCPW resonators an optimal platform for studying collective spin oscillations in different materials. Here we demonstrate coupling between microwave photon mode in an NbN SCPW resonator and magnon modes in an yttrium iron garnet (YIG) sphere.

II. DEVICE FABRICATION AND TRANSPORT MEASUREMENTS

We use intrinsic silicon and sapphire substrates for fabrication of the SCPW resonators. First, the wafers are spin-coated with a bilayer resist consisting of EL9 and PMMA 950 A2. Subsequently, resonator pattern is made by electron beam lithography and developing in a solution of MIBK and IPA in 1:3 volume ratio. NbN is then deposited by reactive DC sputtering with a niobium (Nb) target at a sputtering power of 230 W in presence of continuous flow of 11 sccm of nitrogen and 70 sccm of argon at a sputtering pressure of 6.5×10^{-3} mbar and temperature 120 °C [29]. After sputtering, lift-off is done in acetone to remove the remaining resist along with excess NbN film on top of them. On an NbN film of thickness 80 nm, transport measurements give a $T_C \approx 12.5$ K, $H_C > 14$ T, RRR ≈ 0.9 and room temperature resistivity ≈ 1.95 μΩ m. Variation of resistivity with temperature for the NbN film on intrinsic silicon substrate is shown in Fig. 1. Fig. 1 inset shows SEM image of an NbN film where disorder is clearly visible.

III. DEVICE GEOMETRY AND MICROWAVE MEASUREMENT PROCEDURE

The SCPW resonators are designed in half-wave single port configuration. Fig. 2 (a) shows SEM image of the device. The resonator has a trace width of 28 μm and has been designed from a section of coplanar waveguide with characteristic impedance of 46 Ω on intrinsic silicon, neglecting the surface impedance of the superconducting film. A coupling capacitor is made between input port and the resonator for coupling microwave power in-and-out of the resonator. The measurements are done in a dilution fridge and sufficient number of attenuators are kept at different plates of the fridge in the input line to ensure proper thermalization of microwave photons reaching the sample (more details in the Supplemental Material).

Ratio of reflected to input signal for a one-port capacitively coupled resonator in reflection geometry, as seen in Fig. 2 (a), is described by the reflection coefficient S_{11}. Within the linear response of the resonator, S_{11} as a function of frequency (f),

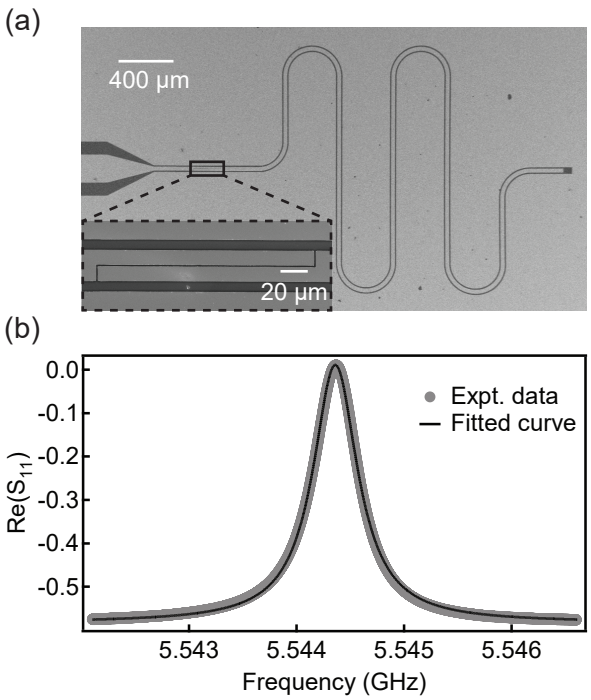

FIG. 2. (a) SEM image of an NbN SCPW resonator [Inset: Zoomed in image of coupling capacitor]. (b) Real part of S_{11} measured at 20 mK temperature along with fitting function.

for a half-wave single port resonator can be modeled by,

$$S_{11}(f) = 1 - \frac{Q_i}{\frac{1}{2}(Q_i + Q_e) + iQ_iQ_e\frac{f-f_0}{f_0}} \tag{1}$$

where Q_i is the internal quality factor, Q_e is the external quality factor and f_0 is the resonance frequency [6]. Fig. 2 (b) shows a representative measurement of the real part of S_{11} taken at 20 mK and zero magnetic field, along with the fitted curve using Eq. 1. This allows us to extract the Q_i for various studies done in this work. We find maximum $Q_i \approx 22000$ at 20 mK temperature and zero magnetic field. We note that Q_e determines the coupling of the resonator to the external measurement circuitry. We have studied resonators which are designed to be overcoupled ($Q_i > Q_e$) and undercoupled ($Q_i < Q_e$) at base temperature and zero magnetic field, to capture variation of Q_i in regimes with different internal loss rates. We have used the in-phase response (real part of S_{11}) to extract out the resonator parameters (details in the Supplemental Material).

IV. CHARACTERIZATION WITH RESPECT TO TEMPERATURE AND MICROWAVE POWER

After establishing the basic characterization procedure, we study the internal loss of the resonator by varying experimental conditions such as drive power, temperature and magnetic field in different orientations; our primary focus is on devices fabricated on intrinsic silicon substrate (characterization for sapphire substrate is included in the Supplemental Material).

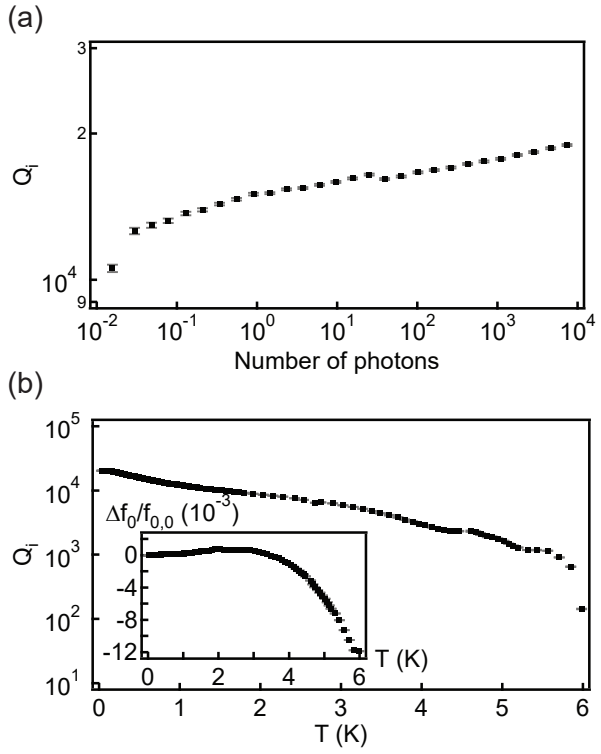

FIG. 3. Characterization of NbN SCPW resonators as a function of microwave power and temperature. (a) and (b) Variation of Q_i with increasing number of microwave photons and temperature, respectively, for intrinsic silicon substrate [Inset of (b): Variation of $\Delta f_0/f_{0,0}$ with temperature for the same]. Note that the error-bars are of size comparable to the markers.

Dependence of resonance characteristics on P_{RF} is performed to investigate the performance of these resonators at and below single photon power level. From Fig. 3 (a) we observe a small increasing trend in Q_i as the mean number of microwave photons in the cavity is increased. Such a behavior suggests the presence of two-level systems (TLS) [35]. At higher power, TLS get saturated and result in higher Q_i. For all the subsequent measurements discussed in the manuscript, we use a measurement power equivalent to approximately 10^3 photons in the resonator. Temperature dependence of the Q_i and $\frac{\Delta f_0}{f_{0,0}}$ (where Δf_0 is shift in resonance frequency from its value at base temperature and zero magnetic field, $f_{0,0}$) has been shown in Fig. 3 ((b) and inset of (b) respectively). As a general trend, above $T \approx 4$ K f_0 of the resonators show a downward shift. This reduction in f_0 can be attributed to the increasing kinetic inductance due to reduction in the number density of available Cooper pairs. Furthermore, for the same reason, increase in number density of quasiparticles causes internal losses to increase, thereby lowering Q_i. A downward shift in the relative frequency shift below $T \approx 1.5$ K confirms the presence of TLS [35].

V. STUDYING DEPENDENCE ON PARALLEL AND PERPENDICULAR MAGNETIC FIELD

As our primary motive is to develop these resonators for magnon coupling experiments [33, 36, 37], it is imperative to characterize their response in magnetic field. Although the resonance frequency of a magnon mode depends on the geometry and the material properties, usually a magnetic field of ~ 100 mT could be sufficient to obtain magnon modes near 5 GHz [32, 33]. Magnetic field dependence of the resonators in orientations parallel (B_{para}) and perpendicular (B_{perp}) to the SCPW plane has been shown in Fig. 4. Fig. 4 (a) and (b) show the color-scale plots of $|S_{11}|^2$ as a function of frequency and magnetic field for an NbN SCPW resonator, with film thickness 72 nm, on intrinsic silicon substrate, for field orientations parallel and perpendicular to the SCPW plane. These measurements have been done in zero-field-cooled condition to address magnetic field induced losses while continuously varying magnetic field, as is required in many applications. Note that here the cavity is designed to be overcoupled at zero magnetic field. In overcoupled regime, $|S_{11}|^2$ shows small variations (however the resonance feature can be clearly seen in the phase response) and hence resonance dip is not visible at zero magnetic field. The dip starts appearing as vortex induced losses show up at higher fields.

Fig. 4 (c) and (d) show the Q_i values extracted from fit using Eq. 1 for resonators in magnetic field orientation parallel and perpendicular to the SCPW plane respectively. Resonators in parallel field show slower decrease in Q_i. This agrees with the fact that all the films have thicknesses below penetration depth. Whereas, for perpendicular field the rate of degradation of Q_i is much faster due to the dominant role of vortex dynamics induced losses over quasiparticle losses [38].

Comparing the data for variation with magnetic field parallel to the SCPW plane, shown in Fig. 4 (c) for 217 nm and 72 nm thick NbN films, we note that the degradation of Q_i is slower for the thinner film as dissipation due to vortex dynamics plays a lesser role and only quasiparticle losses are important; while for the thicker film this is not the case and there is an early onset of vortex dynamics induced losses. NbN films with smaller thicknesses maintain higher Q_i ($> 10^3$) up to higher parallel magnetic field $B_{\mathrm{para}} \approx 1$ T due to lower flux creep. For orientation of magnetic field perpendicular to the plane of the film, $Q_i > 10^3$ is observed up to $B_{\mathrm{perp}} \approx 100$ mT field.

In Fig. 4 (c) and (d) the resonators are overcoupled ($Q_i \gg Q_e$) at zero field. The choice of Q_e for this is good for tracking Q_i up to larger field range, but leads to high error-bars in fits for Q_i in regime of low internal loss, which is realized near zero magnetic field. So, for determining Q_i more precisely in low magnetic field regime, we fabricated another set of resonators with lower coupling capacitor such that $Q_i \lesssim Q_e$ at zero field. Fig. 4 (e) and (f) show the result of analysis for Q_i with this Q_e and we notice that these results are consistent and have smaller fitting errors (additional details in the Supplemental Material).

The near quadratic and linear dispersion trends in Fig. 4 (a) and (b), in orientations parallel and perpendicular to the

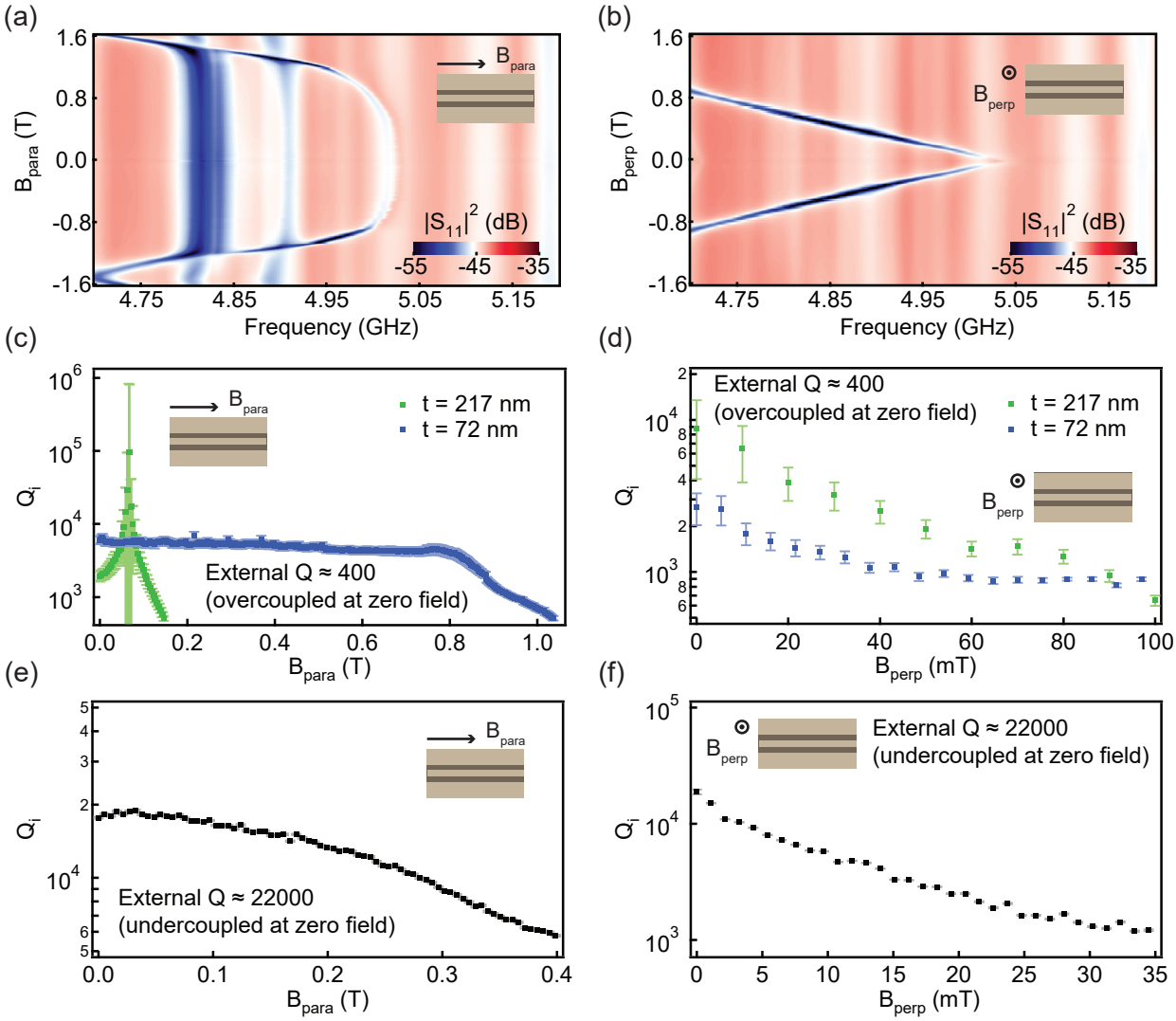

FIG. 4. Characterization of NbN resonators as a function of magnetic field. (a) and (b) Color-scale plots showing variation in $|S_{11}|^2$ for an NbN SCPW resonator with NbN film thickness 72 nm, with frequency and magnetic field for field orientations parallel and perpendicular to the SCPW plane respectively. (c) and (d) Variation of Q_i with magnetic field for film thicknesses 217 nm and 72 nm on intrinsic silicon substrate, for parallel and perpendicular field orientations respectively. These resonators are overcoupled, $Q_i \gg Q_e$, at zero magnetic field; Q_i reduces with increasing magnetic field due to vortex induced losses and eventually goes to undercoupled regime, $Q_i < Q_e$; in undercoupled regime $|S_{11}|^2$ shows a dip at resonance frequency, while for $Q_i \gg Q_e$, change in $|S_{11}|^2$ is minimal. Although Q_i can be tracked up to large magnetic field range using this choice of Q_e, it gives rise to high error-bars in fits for Q_i when $Q_i \gg Q_e$ (near zero field). Another set of resonators with $Q_i \lesssim Q_e$ are studied to accurately determine Q_i near zero field. Dependencies at lower fields are more accurately calculated using these undercoupled resonators having film thickness 80 nm and are shown in (e) and (f) for parallel and perpendicular magnetic fields respectively; here the error-bars have reduced to size comparable to the markers. Measurements were performed at 20 mK temperature.

magnetic field respectively, is well described by Abrikosov-Gor'kov (AG) theory [39]. For SCPW resonators, resonance frequency of the fundamental mode can be written as $f_0 = \frac{\beta}{\sqrt{L_l}}$, where $\beta = \frac{1}{2l\sqrt{C_l}}$ with l, C_l and L_l being the length, capacitance per unit length and inductance per unit length of the resonator. The total inductance contains contribution from the geometric inductance (L_g, per unit length) and the kinetic inductance (L_k, per unit length). As the shift in resonance frequency comes from the kinetic inductance part, it is straight forward to obtain $\frac{\Delta L_k}{L_k} = -\frac{2\beta^2}{\beta^2 - f_0^2 L_g}\frac{\Delta f_0}{f_{0,0}}$ where Δ represents change in associated quantity from its $B = 0$ T value. Now we use the fact that for $T \ll T_C$, $L_k \propto \frac{1}{T_C}$ and $k_B \Delta T_C = -\frac{\pi\alpha}{4}$ where α is the half of depairing energy and for a thin film in perpendicular magnetic field case it can be written as $\alpha = DeB_{\text{perp}}$ [39, 40] where D is the electronic diffusion constant and e is magnitude of electron charge. Using this formalism we fit a straight line $\frac{\Delta f_0}{f_{0,0}} = -kB_{\text{perp}}$ to the dispersion (details in the Supplemental Material) and find D from the relation $D = \frac{8k}{\pi e}\frac{\beta^2 k_B T_C}{\beta^2 - f_0^2 L_g}$. We find $D \approx 5 \times 10^{-4}$ m^{2}s^{-1} which is close to values reported previously [41].

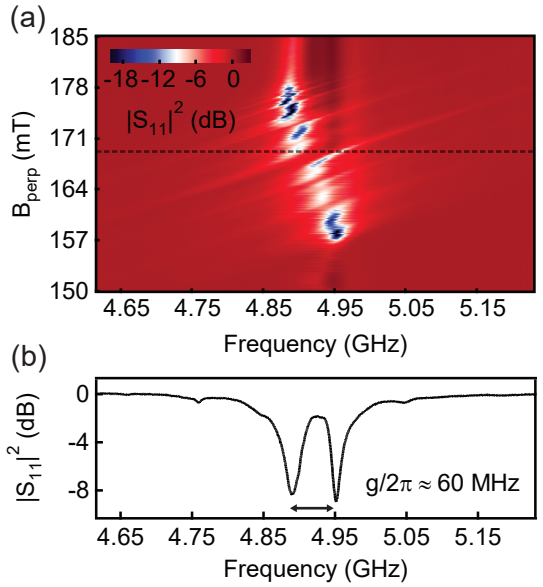

FIG. 5. Observation of strong coupling between magnon modes in an YIG sphere placed at the current antinode of an NbN SCPW resonator (in magnetic field perpendicular to the SCPW plane) and microwave photon mode in the resonator. (a) The color-scale plot of normalized $|S_{11}|^2$ with frequency and magnetic field shows multiple avoided crossings between the cavity photon mode and several magnon modes in the YIG sphere. (b) The line-plot corresponding to $B_{\text{perp}} = 169$ mT (dashed line in (a)) shows the avoided crossing between the SCPW resonator mode and the magnetostatic Kittel mode corresponding to uniform precession of the magnetic moments in YIG with a coupling strength $g/2\pi \approx 60$ MHz.

We observe a weak hysteresis in the measurement depending on the sweep direction of the magnetic field (details in the Supplemental Material). All the measurements presented in Fig. 4 were recorded consistently with an upward sweep direction of the magnetic field. In parallel field orientation, a misalignment between the direction of the magnetic field and the plane of the superconducting film, can also cause losses due to a non-zero out of plane component of the magnetic field. In our experiment, we estimated this misalignment to be less than 1°, as the shift in resonant frequency remains flat for parallel magnetic field up to ≈ 0.8 T.

VI. COUPLING BETWEEN RESONATOR MODE AND MAGNETOSTATIC MODES IN YIG SPHERE

YIG is a ferrimagnetic insulator which sustains magnetostatic modes; resonance frequencies of these modes show dispersion with applied static magnetic field. Coupling between a microwave photon and a magnon (quantum of the magnetostatic modes) takes place through the interaction of the magnetic moments with the RF magnetic field of the microwave photons, which helps in persistent spin precession by overcoming Gilbert damping. Strong coupling between magnons in YIG with microwave photons has been realized in experiments including SCPW resonators [36, 42] as well as 3D cavities [37, 43]. It has been used in various hybrid device schemes [43, 44] and is a topic of interest till date [45–47]. For demonstrating application of our NbN SCPW resonators towards cavity magnonics devices, we placed a YIG sphere of 500 μm diameter at the current antinode of an NbN resonator for coupling the magnons in YIG with the microwave photons in the SCPW resonator. To check this coupling, we monitor the reflection coefficient of the cavity as the magnetic field perpendicular to the sample is swept. Fig. 5 (a) shows multiple avoided crossings between the microwave photon mode of NbN SCPW resonator and several magnon modes of the YIG sphere. We find the coupling strength between the resonator mode and the magnetostatic Kittel mode [48], corresponding to uniform precession of the magnetic moments, to be $g/2\pi \approx 60$ MHz (corresponding coupling strength per Bohr magneton, $g_0/2\pi \approx 0.5$ Hz), as shown in the line-plot in Fig. 5 (b) corresponding to $B_{\text{perp}} = 169$ mT. This is larger than both the microwave photon decay rate of $\kappa_i/2\pi \approx 5$ MHz at 169 mT perpendicular field and the magnon decay rate of $\kappa_m/2\pi \approx 1.12$ MHz [43]; this is the key signature of strong coupling between the microwave photons and the magnons. Using these values, we also find the cooperativity $C \approx \frac{g^2}{\kappa_i \kappa_m} \approx 643$. This shows that our NbN SCPW resonators can be an ideal platform for studying collective spin oscillations in different systems.

VII. CONCLUSION

In this work, we have fabricated NbN SCPW resonators using a simple fabrication process and probed their baseline properties. We see $Q_i > 10^3$ persisting up to perpendicular magnetic field of 100 mT which is two times higher than the previously reported results [28]. Using substrate surface treatments and vortex trapping schemes Q_i of these resonators can be made even higher with better performance possibly up to even higher magnetic fields. Our fabrication protocols have the potential to incorporate exfoliable crystals in the microwave circuits. Furthermore, we have also demonstrated the effectiveness of these resonators in coupling with spin ensembles to study collective spin oscillations and making hybrid quantum devices.

ACKNOWLEDGMENTS

We thank Rajamani Vijayaraghavan, Ipsita Das, Sanat Ghosh, Sudhir Sahu, Suman Kundu, Sumeru Hazra, Ameya Riswadkar, Anirban Bhattacharjee and Srijita Das for helpful discussion and experimental assistance. We also thank Bhagyashree Chalke and Rudheer Bapat for doing SEM imaging. We acknowledge the Swarnajayanti Fellowship of the Department of Science and Technology (for M.M.D.), DST Nanomission grant SR/NM/NS-45/2016, ONRG grant N62909-18-1-2058, and the Department of Atomic Energy of the Government of India for support.

[1] P. K. Day, H. G. LeDuc, B. A. Mazin, A. Vayonakis, and J. Zmuidzinas, Nature **425**, 817 (2003).

[2] E. A. Tholén, A. Ergül, E. M. Doherty, F. M. Weber, F. Grégis, and D. B. Haviland, Applied Physics Letters **90**, 253509 (2007).

[3] M. A. Castellanos-Beltran and K. W. Lehnert, Applied Physics Letters **91**, 083509 (2007).

[4] A. Wallraff, D. I. Schuster, A. Blais, L. Frunzio, R.-S. Huang, J. Majer, S. Kumar, S. M. Girvin, and R. J. Schoelkopf, Nature **431**, 162 (2004).

[5] C. A. Regal, J. D. Teufel, and K. W. Lehnert, Nature Physics **4**, 555 (2008).

[6] V. Singh, S. J. Bosman, B. H. Schneider, Y. M. Blanter, A. Castellanos-Gomez, and G. A. Steele, Nature Nanotechnology **9**, 820 (2014).

[7] Y. Kubo, F. R. Ong, P. Bertet, D. Vion, V. Jacques, D. Zheng, A. Dréau, J.-F. Roch, A. Auffeves, F. Jelezko, J. Wrachtrup, M. F. Barthe, P. Bergonzo, and D. Esteve, Physical Review Letters **105**, 140502 (2010).

[8] R. Amsüss, C. Koller, T. Nöbauer, S. Putz, S. Rotter, K. Sandner, S. Schneider, M. Schramböck, G. Steinhauser, H. Ritsch, J. Schmiedmayer, and J. Majer, Physical Review Letters **107**, 060502 (2011).

[9] V. Ranjan, G. de Lange, R. Schutjens, T. Debelhoir, J. P. Groen, D. Szombati, D. J. Thoen, T. M. Klapwijk, R. Hanson, and L. DiCarlo, Physical Review Letters **110**, 067004 (2013).

[10] J. R. Petta, A. C. Johnson, J. M. Taylor, E. A. Laird, A. Yacoby, M. D. Lukin, C. M. Marcus, M. P. Hanson, and A. C. Gossard, Science **309**, 2180 (2005).

[11] K. C. Nowack, F. H. L. Koppens, Y. V. Nazarov, and L. M. K. Vandersypen, Science **318**, 1430 (2007).

[12] D. I. Schuster, A. P. Sears, E. Ginossar, L. DiCarlo, L. Frunzio, J. J. L. Morton, H. Wu, G. A. D. Briggs, B. B. Buckley, D. D. Awschalom, and R. J. Schoelkopf, Physical Review Letters **105**, 140501 (2010).

[13] H. Malissa, D. I. Schuster, A. M. Tyryshkin, A. A. Houck, and S. A. Lyon, Review of Scientific Instruments **84**, 025116 (2013).

[14] O. W. B. Benningshof, H. R. Mohebbi, I. A. J. Taminiau, G. X. Miao, and D. G. Cory, Journal of Magnetic Resonance **230**, 84 (2013).

[15] F. E. Schmidt, M. D. Jenkins, K. Watanabe, T. Taniguchi, and G. A. Steele, Nature Communications **9**, 1 (2018).

[16] J. G. Kroll, W. Uilhoorn, K. L. v. d. Enden, D. d. Jong, K. Watanabe, T. Taniguchi, S. Goswami, M. C. Cassidy, and L. P. Kouwenhoven, Nature Communications **9**, 1 (2018).

[17] J. I.-J. Wang, D. Rodan-Legrain, L. Bretheau, D. L. Campbell, B. Kannan, D. Kim, M. Kjaergaard, P. Krantz, G. O. Samach, F. Yan, J. L. Yoder, K. Watanabe, T. Taniguchi, T. P. Orlando, S. Gustavsson, P. Jarillo-Herrero, and W. D. Oliver, Nature Nanotechnology **14**, 120 (2019).

[18] C. Gong and X. Zhang, Science **363**, eaav4450 (2019).

[19] V. Singh, B. H. Schneider, S. J. Bosman, E. P. J. Merkx, and G. A. Steele, Applied Physics Letters **105**, 222601 (2014).

[20] V. E. Calado, S. Goswami, G. Nanda, M. Diez, A. R. Akhmerov, K. Watanabe, T. Taniguchi, T. M. Klapwijk, and L. M. K. Vandersypen, Nature Nanotechnology **10**, 761 (2015).

[21] D. J. van Woerkom, A. Geresdi, and L. P. Kouwenhoven, Nature Physics **11**, 547 (2015).

[22] M. R. Vissers, J. Gao, D. S. Wisbey, D. A. Hite, C. C. Tsuei, A. D. Corcoles, M. Steffen, and D. P. Pappas, Applied Physics Letters **97**, 232509 (2010).

[23] F. W. Carter, T. Khaire, C. Chang, and V. Novosad, Applied Physics Letters **115**, 092602 (2019).

[24] C. Song, T. W. Heitmann, M. P. DeFeo, K. Yu, R. McDermott, M. Neeley, J. M. Martinis, and B. L. T. Plourde, Physical Review B **79**, 174512 (2009).

[25] A. Ghirri, C. Bonizzoni, D. Gerace, S. Sanna, A. Cassinese, and M. Affronte, Applied Physics Letters **106**, 184101 (2015).

[26] C. Song, M. P. DeFeo, K. Yu, and B. L. T. Plourde, Applied Physics Letters **95**, 232501 (2009).

[27] D. Bothner, T. Gaber, M. Kemmler, D. Koelle, and R. Kleiner, Applied Physics Letters **98**, 102504 (2011).

[28] J. Kroll, F. Borsoi, K. van der Enden, W. Uilhoorn, D. de Jong, M. Quintero-Pérez, D. van Woerkom, A. Bruno, S. Plissard, D. Car, E. Bakkers, M. Cassidy, and L. Kouwenhoven, Physical Review Applied **11**, 064053 (2019).

[29] S. P. Chockalingam, M. Chand, J. Jesudasan, V. Tripathi, and P. Raychaudhuri, Physical Review B **77**, 214503 (2008).

[30] M. Mondal, A. Kamlapure, M. Chand, G. Saraswat, S. Kumar, J. Jesudasan, L. Benfatto, V. Tripathi, and P. Raychaudhuri, Physical Review Letters **106**, 047001 (2011).

[31] A. Kamlapure, M. Mondal, M. Chand, A. Mishra, J. Jesudasan, V. Bagwe, L. Benfatto, V. Tripathi, and P. Raychaudhuri, Applied Physics Letters **96**, 072509 (2010).

[32] D. MacNeill, J. T. Hou, D. R. Klein, P. Zhang, P. Jarillo-Herrero, and L. Liu, Physical Review Letters **123**, 047204 (2019).

[33] X. Zhang, C.-L. Zou, L. Jiang, and H. X. Tang, Physical Review Letters **113**, 156401 (2014).

[34] H. H. Kim, B. Yang, S. Li, S. Jiang, C. Jin, Z. Tao, G. Nichols, F. Sfigakis, S. Zhong, C. Li, S. Tian, D. G. Cory, G.-X. Miao, J. Shan, K. F. Mak, H. Lei, K. Sun, L. Zhao, and A. W. Tsen, Proceedings of the National Academy of Sciences **116**, 11131 (2019).

[35] J. Gao, M. Daal, A. Vayonakis, S. Kumar, J. Zmuidzinas, B. Sadoulet, B. A. Mazin, P. K. Day, and H. G. Leduc, Applied Physics Letters **92**, 152505 (2008).

[36] H. Huebl, C. W. Zollitsch, J. Lotze, F. Hocke, M. Greifenstein, A. Marx, R. Gross, and S. T. B. Goennenwein, Physical Review Letters **111**, 127003 (2013).

[37] Y. Tabuchi, S. Ishino, T. Ishikawa, R. Yamazaki, K. Usami, and Y. Nakamura, Physical Review Letters **113**, 083603 (2014).

[38] S. Kwon, A. Fadavi Roudsari, O. W. B. Benningshof, Y.-C. Tang, H. R. Mohebbi, I. A. J. Taminiau, D. Langenberg, S. Lee, G. Nichols, D. G. Cory, and G.-X. Miao, Journal of Applied Physics **124**, 033903 (2018).

[39] M. Tinkham, *Introduction to Superconductivity*, Dover Books on Physics Series (Dover Publications, 2004).

[40] N. Samkharadze, A. Bruno, P. Scarlino, G. Zheng, D. P. DiVincenzo, L. DiCarlo, and L. M. K. Vandersypen, Physical Review Applied **5**, 044004 (2016).

[41] M. Mondal, A. Kamlapure, S. C. Ganguli, J. Jesudasan, V. Bagwe, L. Benfatto, and P. Raychaudhuri, Scientific Reports **3**, 1357 (2013).

[42] R. G. E. Morris, A. F. v. Loo, S. Kosen, and A. D. Karenowska, Scientific Reports **7**, 1 (2017).

[43] X. Zhang, C.-L. Zou, L. Jiang, and H. X. Tang, Science Advances **2**, e1501286 (2016).

[44] Y. Tabuchi, S. Ishino, A. Noguchi, T. Ishikawa, R. Yamazaki, K. Usami, and Y. Nakamura, Science **349**, 405 (2015).

[45] Y. Li, T. Polakovic, Y.-L. Wang, J. Xu, S. Lendinez, Z. Zhang, J. Ding, T. Khaire, H. Saglam, R. Divan, J. Pearson, W.-K.

Kwok, Z. Xiao, V. Novosad, A. Hoffmann, and W. Zhang, Physical Review Letters **123**, 107701 (2019).
[46] J. T. Hou and L. Liu, Physical Review Letters **123**, 107702 (2019).
[47] L. McKenzie-Sell, J. Xie, C.-M. Lee, J. W. A. Robinson, C. Ciccarelli, and J. A. Haigh, Physical Review B **99**, 140414 (2019).
[48] C. Kittel, Physical Review **110**, 1295 (1958).
[49] D. Bothner, T. Gaber, M. Kemmler, D. Koelle, R. Kleiner, S. Wünsch, and M. Siegel, Physical Review B **86**, 014517 (2012).
[50] L. Ji, M. S. Rzchowski, N. Anand, and M. Tinkham, Physical Review B **47**, 470 (1993).
[51] P. Raychaudhuri, Superconductor Science and Technology **9**, 447 (1996).

SUPPLEMENTAL MATERIAL

SI. SCHEMATIC FOR MEASUREMENT CIRCUIT

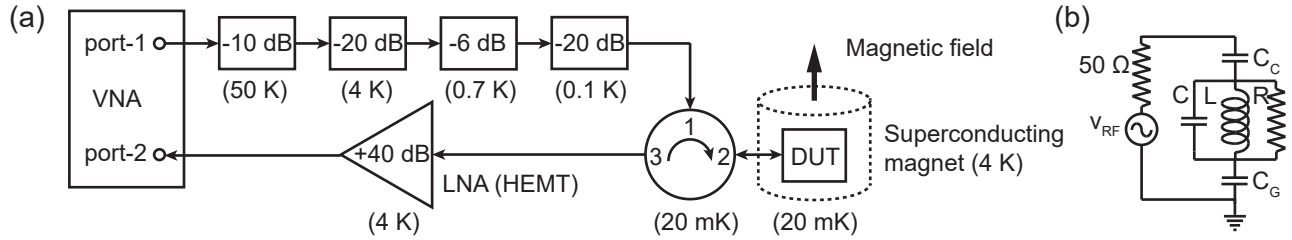

FIG. S1. (a) Circuit schematic for reflection measurement of NbN SCPW resonators in an Oxford Triton dilution fridge. RF signal from one port of a VNA is carried through a coax line with attenuation at different temperature plates inside the fridge and to the device under test (DUT) through a circulator. Reflected signal from the device is amplified by a Low Noise Factory HEMT amplifier at 4 K plate before sending it back to the other port of the VNA. (b) A lumped element equivalent of the device. Here the parallel combination of L, C and R represent the resonator, C_C represents the coupling capacitor, C_G is a capacitor representing the open-to-ground configuration of the one-port resonator and v_{RF} represents the VNA, which is used for actuation and measurement of the resonator.

Fig. S1 (a) shows schematic of the circuit for reflection measurement of the NbN SCPW resonators. Measurements are done in an Oxford Triton dilution fridge containing a superconducting magnet. Input line of the RF signal includes several attenuators at different stages of the fridge as shown, for proper thermalization of the microwave photons reaching the sample. Input and output paths are separated using a circulator from Quinstar (OXE89 CTH0408KC) before the device. Amplification is done by a Low Noise Factory amplifier (LNF-LNC0.3_14A) attached to the 4 K plate of the fridge. Attained base temperature at sample is 20 mK. The superconducting coil around the sample is used to apply magnetic field. The measurements are done using an Anritsu (MS46122B) vector network analyzer (VNA). Fig. S1 (b) shows a lumped element equivalent to the device.

SII. COMPARISON BETWEEN OVERCOUPLED AND UNDERCOUPLED RESONATORS

Proper designing of coupling capacitor (C_C) is essential in extracting internal Q of the resonators accurately in regimes with different internal loss rates. Reflection coefficient (S_{11}) of a one-port resonator as a function of frequency is given by

$$S_{11}(f) = 1 - \frac{k_e}{\frac{k_i+k_e}{2} + i(f-f_0)} \tag{S1}$$

where $k_i = \kappa_i/2\pi$ and $k_e = \kappa_e/2\pi$ are internal and external loss rates respectively and f_0 is the resonance frequency of the resonator [6]. They are related to internal Q (Q_i) and external Q (Q_e) by $Q_i = 2\pi\frac{f_0}{\kappa_i} = \frac{f_0}{k_i}$ and $Q_e = 2\pi\frac{f_0}{\kappa_e} = \frac{f_0}{k_e}$. Note that an overall constant phase factor to S_{11} with 0 or π phase can give rise to a dip or peak respectively in the real part of S_{11}, which are equivalent. For understanding effect of chosen Q_e in accuracy of extracted Q_i using Eq. (S1), we do numeric calculations in Mathematica, as shown in Fig. S2. Greater shift in peak height (Δh) of real part of S_{11} for same Q_i variation provides higher accuracy in estimation of Q_i. Fig. S2 (a) and (b) show variation in Δh in high Q_i (i.e. low k_i) regime for high (10 MHz) and low (0.1 MHz) values of chosen k_e respectively. For the higher values of Q_i considered in Fig. S2, these correspond to overcoupled ($Q_i > Q_e$) and undercoupled ($Q_i < Q_e$) designs respectively. High Q_i regime is realized near base temperature of 20 mK and zero magnetic field. Fig. S2 (c) and (d) show variation in Δh in low Q_i (i.e. high k_i) regime for these two choices of k_e. Low Q_i regime is realized as losses are introduced in the system due to increase in temperature and/or magnetic field. Fig. S2 (e) shows

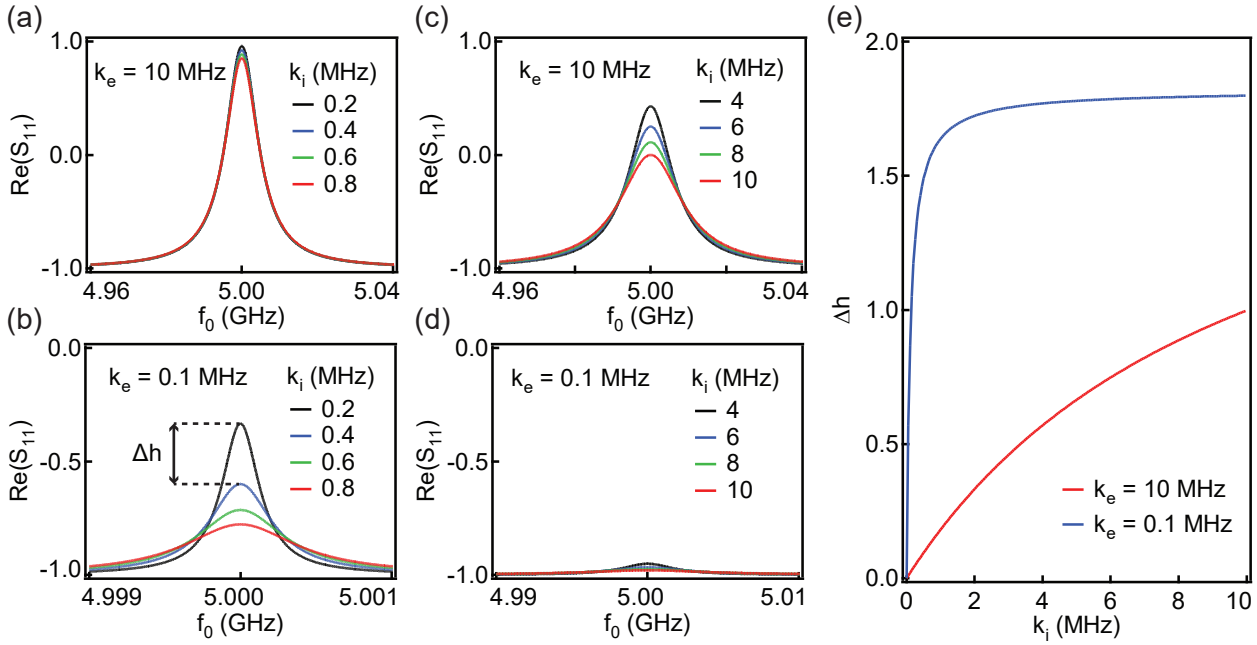

FIG. S2. Numeric calculations showing shift in peak height Δh of real part of S_{11}. (a) and (b) show Δh in high Q_i (low k_i) regime for resonator designs with low ($k_e = 10$ MHz) and high ($k_e = 0.1$ MHz) Q_e values respectively (i.e. overcoupled and undercoupled respectively). (c) and (d) show Δh in low Q_i (low k_i) regime for resonators with these two designs respectively. (e) shows a comparison between these two designs of k_e at different k_i. From these plots we observe that an overcoupled design is preferable for good fit in low Q_i regime and an undercoupled design is preferable for good fit in high Q_i regime.

a comparison between $k_e = 10$ MHz and $k_e = 0.1$ MHz in terms of variation of Δh with k_i. From these panels we note that in the high Q_i regime undercoupled design (low k_e with $k_e < k_i$) is preferable for good fit, whereas in the low Q_i regime overcoupled design (high k_e with $k_e > k_i$) is preferable for good fit. We use resonators with $Q_e \approx 400$ and $Q_e \approx 22000$ for characterization of the resonators. We find that although lower Q_e is useful for extracting Q_i up to higher magnetic fields it gives high errorbars in the lower magnetic fields. Whereas, using higher Q_e enables us to extract Q_i with higher accuracy in low magnetic field regime, as implied by much lower error bars as shown in main text (Fig.4). This agrees with our comparison in Fig. S2.

SIII. SIMULTANEOUS FITTING TO REAL AND IMAGINARY PARTS OF S_{11}

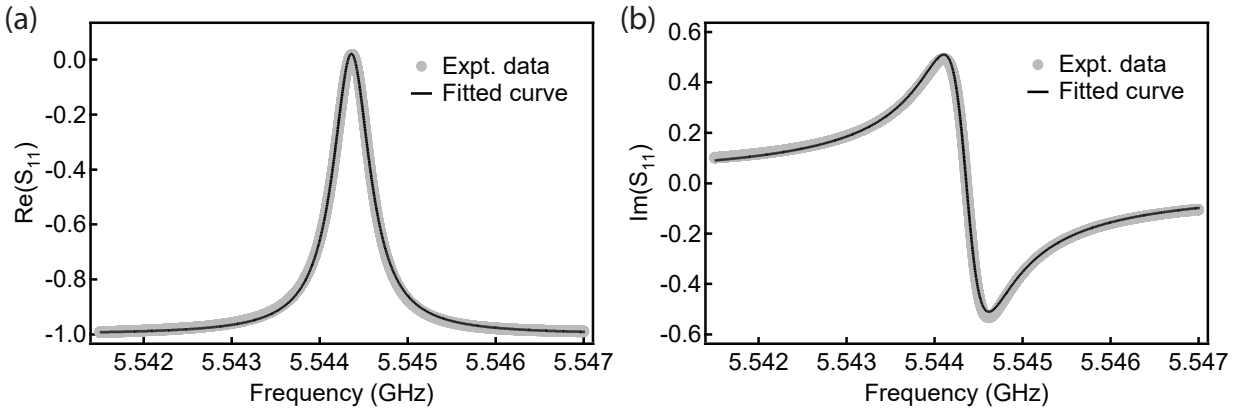

FIG. S3. (a) and (b) Simultaneous fit to real and imaginary parts of S_{11} respectively, of normalized experimental data for an NbN SCPW resonator at zero magnetic field and 20 mK base temperature using Eq. S1.

We have extracted system parameters by fitting to the real part of S_{11} data using Eq. S1. Simultaneous fitting to both real and

imaginary part of S_{11} is also possible for slight improvement. Fig. S3 (a) and (b) show the simultaneous fits to real and imaginary parts of normalized S_{11} obtained from measurement of a resonator with $Q_e \approx Q_i \approx 22000$; this is close to the value obtained by fitting only to the real part of S_{11} as mentioned in main text. Further improvement can be done by implementing ways of continuous background calibration during magnetic field sweep to eliminate the background, which shows slight variation with increasing magnetic field, from the measured signal.

SIV. COMPARISON WITH PREVIOUS REPORTS

TABLE SI. Comparison of Q_i variation with magnetic field with previous reports

Material	Resonator geometry	Flux trapping scheme	Max B_{para} (for $Q_i > 10^3$)	Max B_{perp} (for $Q_i > 10^3$)
Nb [38]	SCPW	No	2.7 T (loaded $Q > 10^3$)	24 mT (loaded $Q > 2.5 \times 10^4$)
NbTiN [28]	SCPW	Yes	6 T ($Q_i > 10^5$)	45 mT (20 mT for $Q_i > 10^5$)
NbTiN nanowire [40]	Nanowire	No	6 T ($Q_i > 2 \times 10^5$)	400 mT ($Q_i > 10^4$)
NbN (our work)	SCPW	No	1 T	100 mT

Table SI shows a comparison of highest applied magnetic field, in orientations parallel and perpendicular to the SCPW plane, up to which $Q_i > 10^3$ is retained, with previous reports for other type-II superconductors. We observe that even in absence of any substrate surface treatment and flux trapping schemes, our NbN resonators retain $Q_i > 10^3$ up to parallel fields comparable to and perpendicular field twice the maximum value reported previously for an SCPW resonator. Further implementation of substrate surface treatments and flux trapping schemes are expected to increase this maximum field of high Q_i retention even more.

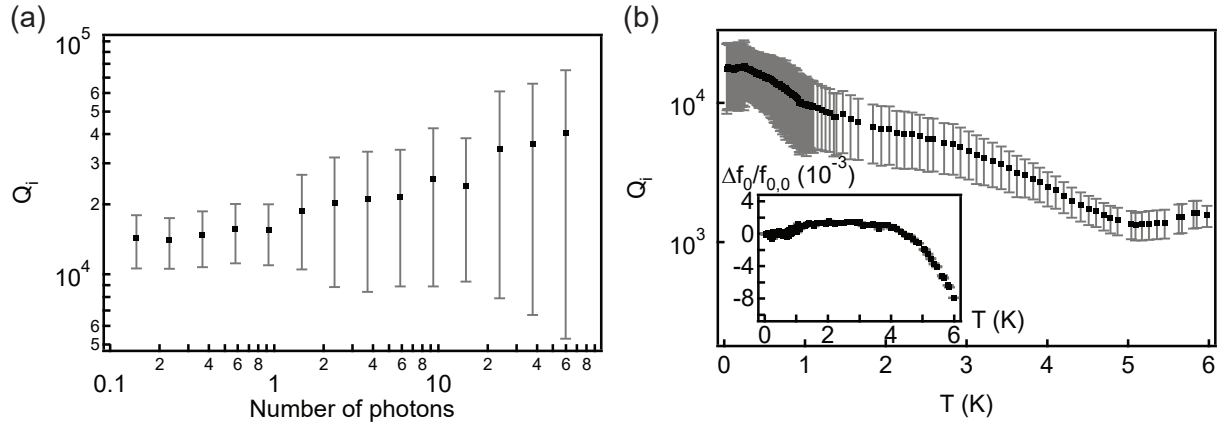

FIG. S4. (a) and (b) Variation of Q_i with microwave power and temperature for an NbN SCPW resonator with film thickness 94 nm on sapphire substrate, respectively [Inset of (b): variation of $\Delta f_0/f_{0,0}$ with temperature for the same].

SV. CHARACTERIZATION OF RESONATORS ON SAPPHIRE SUBSTRATE WITH MICROWAVE POWER AND TEMPERATURE

Fig. S4 (a) and (b) show variation of Q_i of an NbN SCPW resonator on sapphire substrate with a film thickness of 94 nm with microwave power and temperature respectively. Inset of Fig. S4 (b) shows variation of $\Delta f_0/f_{0,0}$ with temperature. We note that the variations are similar to intrinsic silicon substrate as shown in main text.

SVI. CHARACTERIZATION OF RESONATORS ON SAPPHIRE SUBSTRATE WITH MAGNETIC FIELD

Fig. S5 (a) and (b) show variation of Q_i and $\Delta f_0/f_{0,0}$ with magnetic field parallel (B_{para}) and perpendicular (B_{perp}) to the SCPW plane respectively. This dependence is similar to that of resonators on intrinsic silicon substrate as shown in main text.

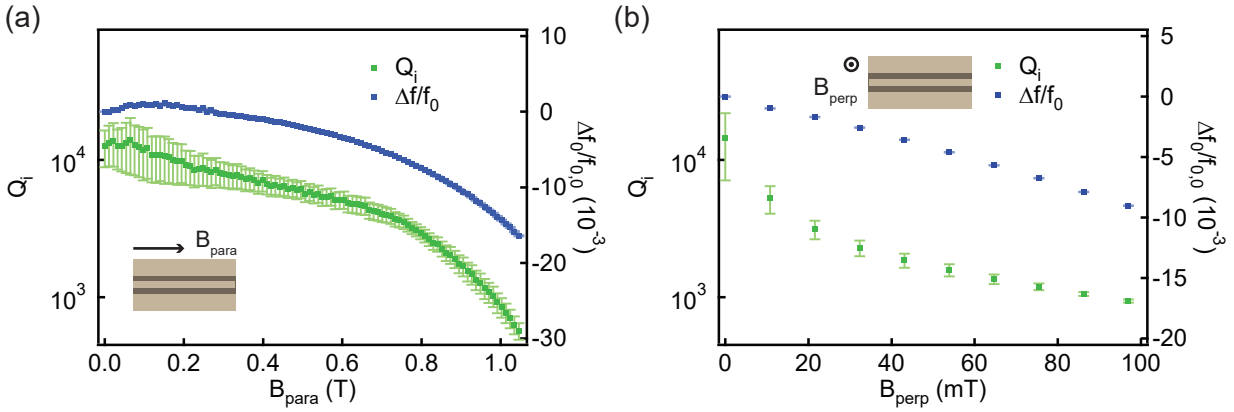

FIG. S5. Characterization of an NbN SCPW resonator on sapphire substrate (NbN film thickness 94 nm) as a function of magnetic field. (a) and (b) Variation of Q_i and $\Delta f_0/f_{0,0}$ for parallel and perpendicular field orientations respectively.

SVII. VARIATION IN $\Delta f_0/f_{0,0}$ WITH MAGNETIC FIELD FOR RESONATORS ON INTRINSIC SILICON SUBSTRATE

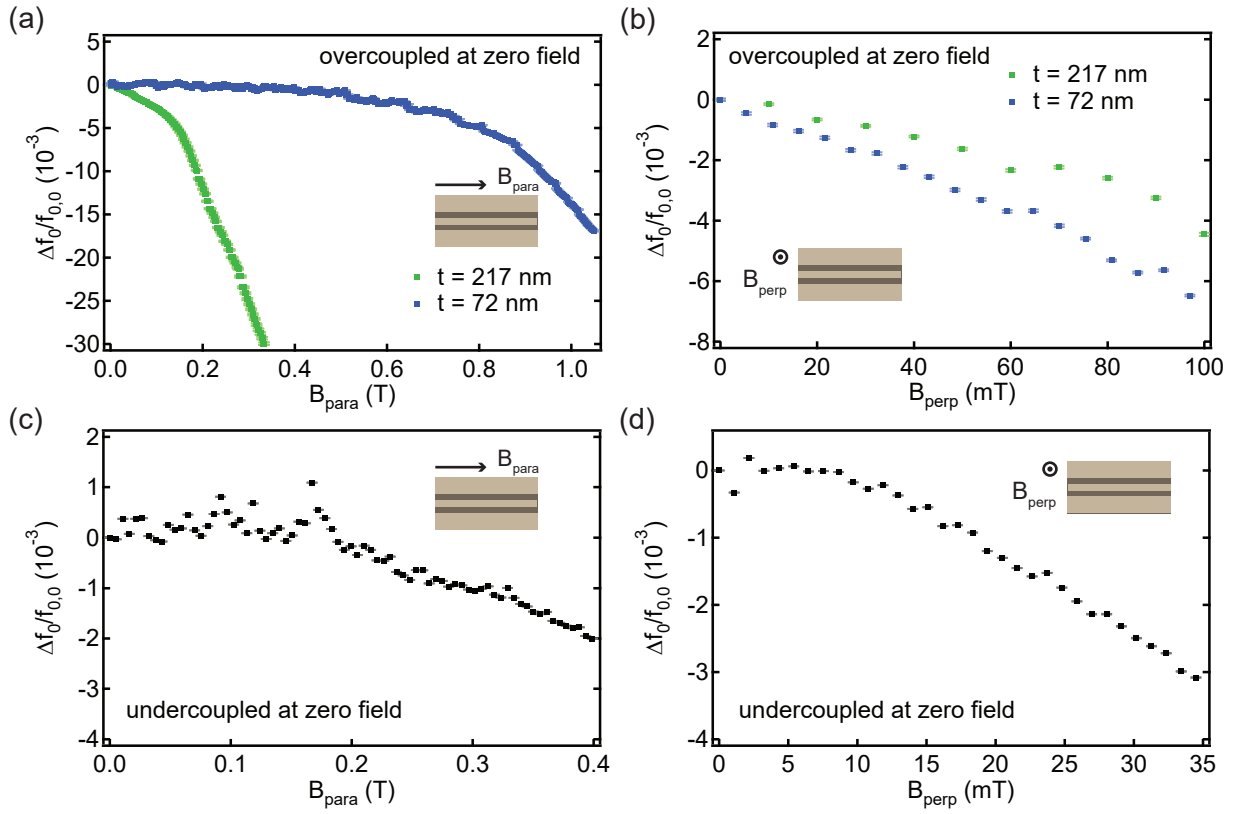

FIG. S6. Relative shift in resonance frequency $\Delta f_0/f_{0,0}$ of NbN resonators on intrinsic silicon substrate. (a) and (b) Variation in $\Delta f_0/f_{0,0}$ for the overcoupled resonators with NbN film thicknesses 217 nm and 72 nm in parallel and perpendicular magnetic field respectively. (c) and (d) Variation in $\Delta f_0/f_{0,0}$ for the undercoupled resonators with NbN film thickness 80 nm in parallel and perpendicular magnetic field respectively.

Fig. S6 (a) and (b) show the variation of $\Delta f_0/f_{0,0}$ for resonators on intrinsic silicon substrate with film thicknesses 217 nm and 72 nm with magnetic field parallel and perpendicular to the SCPW plane respectively. These show the nearly quadratic and linear dispersion of resonance frequency in parallel and perpendicular magnetic field respectively. The slope of the linear dispersion has been used to calculate electronic diffusion constant D. Fig. S6 (c) and (d) show the same for resonators with undercoupled design.

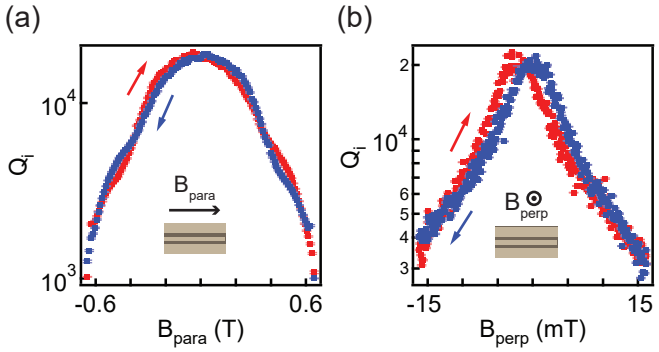

FIG. S7. Hysteresis in NbN SCPWs with magnetic field. (a) and (b) Hysteresis in an NbN SCPW resonator on intrinsic silicon substrate with respect to direction of magnetic field sweep, with field parallel and perpendicular to the SCPW respectively.

SVIII. HYSTERESIS WITH MAGNETIC FIELD

We observe some amount of hysteresis in the NbN SCPW resonators depending upon the direction of magnetic field sweep. Fig. S7 (a) and (b) show hysteresis in Q_i of a resonator on intrinsic silicon substrate. We observe that for the perpendicular field, Q_i is higher in down-sweep of field compared to the up-sweep; whereas, for the parallel field, we observe regimes with higher as well as lower Q_i in down-sweep compared to up-sweep. The perpendicular field case is similar to previous report and is similar to prediction from Norris-Brandt-Indenbom (NBI) model with inhomogeneous current density [49]. But the presence of two regimes in case of parallel field sweep suggests the presence of grain boundaries [50, 51] in the NbN film, which is also apparent from the SEM image of an NbN film as shown in the inset of Fig.1 in the main text.

SIX. LINEAR FIT FOR FINDING D

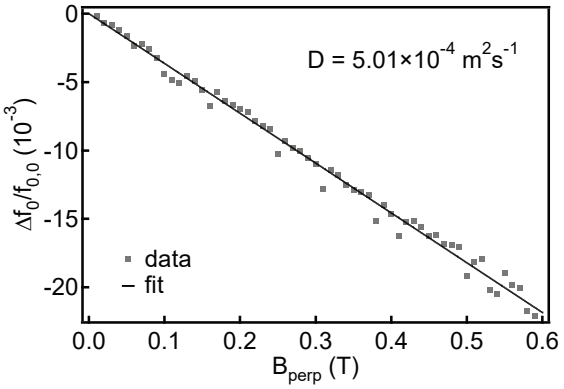

FIG. S8. Linear fit to the $\frac{\Delta f_0}{f_{0,0}}$ vs B_{perp} data for determination of electronic diffusion constant (D) for an NbN SCPW resonator on intrinsic silicon substrate.

The electronic diffusion constant (D) is given by $D = \frac{8k}{\pi e}\frac{\beta^2 k_B T_C}{\beta^2 - f_0^2 L_g}$ as described in main text, where k is the negative of slope of $\frac{\Delta f_0}{f_{0,0}}$ vs B_{perp} plot. Fig. S8 shows a linear fit to the $\frac{\Delta f_0}{f_{0,0}}$ vs B_{perp} data for an NbN SCPW resonator on intrinsic silicon substrate. The estimated electronic diffusion constant is $D = 5.01 \times 10^{-4}$ m^{2}s^{-1}.